

Synchrotron X-ray and *ab initio* studies of β -Si₃N₄D. du Boulay,^a N. Ishizawa,^{a*} T. Atake,^b V. Streltsov,^c K. Furuya^d and F. Munakata^e

^aCeramics Research Laboratory, Nagoya Institute of Technology, Asahigaoka, Tajimi 507-0071, Japan, ^bMaterials and Structures Laboratory, Tokyo Institute of Technology, 4259 Nagatsuta-cho Midori-ku, Yokohama 226-8503, Japan, ^cCSIRO Health Sciences and Nutrition, 343 Royal Parade, Parkville VIC 3052, Australia, ^dSeimi Chemical Co. Ltd, 3-2-10 Chigasaki, Chigasaki-city, Kanagawa, 253-8585, Japan, and ^eGraduate School of Engineering, Yokohama National University, 79-5 Tokiwadai, Hodogaya-ku, Yokohama 240-8501, Japan

Correspondence e-mail: ishizawa@nitech.ac.jp

Almost absorption- and extinction-free single-crystal synchrotron X-ray diffraction data were measured at 150, 200 and 295 K for β -Si₃N₄, silicon nitride, at a wavelength of 0.7 Å. The true symmetry of this material has been the subject of minor controversy for several decades. No compelling evidence favouring the low-symmetry *P*6₃ model was identified in this study.

Received 16 March 2004

Accepted 9 June 2004

1. Introduction

Silicon nitride is a well known refractory ceramic that commonly occurs as an amorphous phase (Matsunaga *et al.*, 2000; Matsunaga & Iwamoto, 2001), or in two well characterized hexagonal phases denoted as alpha and beta (Grün, 1979). The non-centrosymmetric and slightly less dense alpha phase (3.149 Mg m⁻³) undergoes an irreversible first-order phase transition to the beta phase (3.203 Mg m⁻³) upon heating to high temperature and thereafter decomposes at around 2000 K (Schneider *et al.*, 1994). Owing to its properties of strength and hardness (bulk modulus of 259 GPa; Vogelgesang *et al.*, 2000; Ogata *et al.*, 2003) Si₃N₄ finds use in many industrial applications where high-temperature stability, resistance to wear and durability are important. Its use in these applications is strongly dependent on its microstructural properties, such as grain sizes and shapes, and the manner in which they weld together. These properties in turn are intimately related to the underlying structural chemistry.

Silicon nitride is also used in the electronics industry for protective coatings owing to its resistance to both oxygen diffusion and oxidation. Its higher dielectric constant, density and radiation hardness in comparison with SiO₂ is also advantageous for interface layers (Zhao & Bachlechner, 1998). The SIALON substitutional Si_{6-z}Al_zO_zN_{8-z} ceramic solid solutions of the α and β phases also have useful properties which, although less resilient than the silicon nitride prototype, can be tuned to specific purposes over a wide range (Jack & Wilson, 1972; Ching, Huang & Mo, 2000).

Liu & Cohen (1989) stimulated new interest in the beta phase when they calculated that a β -C₃N₄ analogue of β -Si₃N₄ could have a bulk modulus of 427 GPa, comparable to that of diamond (444.8 GPa; Liu & Cohen, 1990). This analogue was envisaged as a prime candidate for the next generation of super-hard and super-wear-resistant materials (Vogelgesang *et al.*, 2000), although to date its existence and properties are unsubstantiated.

More recently, the report (Zerr *et al.*, 1999) of a possible new cubic spinel phase grown above 2000 K and 15 GPa has

Table 1Lattice parameters reported for β -Si₃N₄.

Conditions	Symmetry	Temperature (K)	<i>a</i> (Å)	<i>c</i> (Å)
Single-crystal X-ray ^a		150	7.6020 (2)	2.9060 (1)
Single-crystal X-ray ^a		200	7.6015 (3)	2.9061 (1)
Single-crystal X-ray ^a		295	7.6044 (1)	2.9063 (1)
Powder X-ray ^b	<i>P</i> 6 ₃	297	7.60182 (7)	2.90713 (3)
Single-crystal X-ray ^c	<i>P</i> 6 ₃ / <i>m</i>	297	7.607	2.911
Single-crystal X-ray ^d	<i>P</i> 6 ₃	293	7.595 (1)	2.9023 (6)
DFT ^e	<i>P</i> 6 ₃ / <i>m</i>	–	7.5620 (15)	2.8930 (7)
OLCAO dynamics ^f	<i>P</i> 6 ₃ / <i>m</i>	–	7.6220	2.9102
OLCAO dynamics ^f	<i>P</i> 6 ₃	–	7.6226	2.9014

References: (a) current work; (b) Schneider *et al.* (1994); (c) Borgen & Seip (1961); (d) Grün (1979); (e) Belkada *et al.* (2000); (f) Ching, Ouyang & Gale (2000).

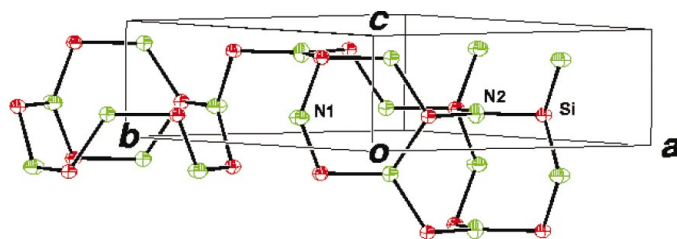
Table 2

Data measurement parameters and symmetry-model independent corrections and statistics.

	Crystal (1)	Crystal (2)	Crystal (2)
Temperature (K)	295	200	150
Wavelength (Å)	0.7502	0.7504	0.7504
Cell refinement	21 (2 θ < 128)	12 (2 θ < 112)	12 (2 θ < 112)
<i>R</i> _{cell} †	0.0445 (19 parameters)	0.1259 (10 parameters)	0.0720 (10 parameters)
Scan mode	$\omega/2\theta$	$\omega/2\theta$	$\omega/2\theta$
Scan width (°)	0.30	0.55	0.55
Bg time (s)	0.3	1	0.3
Scan time (s)	3.6	4.4	4.4
Standards (every 94 references)	6	6	6
<i>N</i> _{refl}	8410	12 331	8549
<i>S</i> _{max} full sphere	1.21	1.24	1.21
Transmission	0.9395–0.9390	0.9719–0.9319	0.9719–0.9319
<i>N</i> _{unique}	796	870	796
<i>R</i> _{int} (pre)	0.0245	0.0287	0.0283
Absorption shape	Sphere	Plate	Plate
<i>R</i> _{int} (post)	0.0245	0.0276	0.0272

† From a least-squares fit of the orienting reflections to a hexagonal cell.

renewed interest in silicon nitrides. This is because they contain Si octahedrally coordinated by N and also because density functional theory (DFT) calculations have shown that the spinel bandgap (3.45 eV) should therefore be much lower than that of the β phase (4.6 eV). The corresponding calculations for the hypothetical *c*-C₃N₄ spinel indicate a band gap of 1.14 eV, leading to suggestions by Mo *et al.* (1999) that mixed-phase (C,Si)₃N₄ materials could have their bandgaps tuned for use in solid-state violet or ultraviolet lasers. DFT

**Figure 1**

ORTEP (Johnson, 1971) plot of an extended β -Si₃N₄ unit cell rendered at the 99.9% probability level.

calculations for these materials also indicate rather large bulk moduli for *c*-Si₃N₄ (280 GPa) and *c*-C₃N₄ (369 GPa).

Despite all these new and exciting properties in related materials, a residual uncertainty exists concerning the true symmetry of the fundamental reference material β -Si₃N₄, an uncertainty which we hoped to address here.

Historically, Hardie & Jack (1957) first reported an approximate structure with a symmetry of *P*6₃/*m*. Borgen & Seip (1961) redetermined the structure assuming the same *P*6₃/*m* symmetry. Wild *et al.* (1972) subsequently improved the accuracy of the structure with slightly different coordinates. Thereafter, Grün (1979) proposed a slightly different structure with the non-centrosymmetric space group of *P*6₃. Goodman & O'Keeffe (1980) attempted to resolve this issue using convergent-beam electron diffraction (CBED), concluding that *P*6₃/*m* was the correct symmetry and that atomic displacements of the order implied by Grün could be excluded. In a followup CBED study (Bando, 1983) it was suggested that for very thin samples the symmetry was compatible with *P*6₃/*m*, but with increasing thickness the weakly contributing but non-centrosym-

metric N-atom component of the scattering potential becomes enhanced, revealing the true space group as *P*6₃. Schneider *et al.* (1994) employed X-ray powder diffraction and concurred with Bando and Grün that *P*6₃ gave a statistically significant (Hamilton, 1965) improvement in the structural model, although in the absence of anisotropic displacement parameters. More recently, Ching, Huang & Mo (2000) employed *ab initio* total-energy density functional theory (DFT) calculations involving orthogonalized linear combinations of atomic orbitals (OLCAO) to optimize the β -Si₃N₄ geometry. Their results indicated a slightly lower total energy for the non-centrosymmetric *P*6₃ symmetry (−1415.326 eV per formula unit) in comparison with the centred lattice (−1415.088 eV per formula unit). Thereafter, Belkada *et al.* (2002) used pseudopotential DFT lattice-relaxation techniques, finding minimal energy and thereby structural stability for the *P*6₃/*m* lattice. The controversy therefore continues.

Clearly the underlying structural geometry of β -Si₃N₄, shown in Fig. 1, has been well known and understood for many years. At its lowest level it is essentially a network of trigonally coordinated N and tetrahedrally coordinated Si atoms, each bound solely to atoms of the alternate species. These

Table 3

Observed mean normalized structure factors and expected values for randomly distributed centrosymmetric and non-centrosymmetric structures.

	$ E $	$ E^2 $	$ E^2 - 1 $	$ E^2 - 1 ^2$	$ E^2 - 1 ^3$
Random $P\bar{1}$	0.798	1.000	0.968	2.000	8.000
295 K	0.818	1.000	0.926	1.551	4.546
200 K	0.816	1.000	0.928	1.555	4.494
150 K	0.818	1.000	0.923	1.534	4.424
Random $P1$	0.886	1.000	0.736	1.000	2.000

geometries are quite consistent with sp^2 and sp^3 covalent binding configurations for N and Si, respectively. At a higher level of complexity, the atoms and bond vectors form a network of intermeshed 12-, eight- and six- membered ring systems. The 12-membered rings have a diameter of ~ 5.0 Å and form channels along **c** in association with a series of elongated, eight-membered chair-conformation rings with a minimum diameter of ~ 3.0 Å. Other eight- and six-membered rings are oriented perpendicular to (001), building up the lattice structure along **c**. The six-membered rings have five coplanar atoms, with the sixth atom puckered out of the plane, and have a minimum diameter of $\sim c = 2.9$ Å. Both the alpha and beta phases are laminar in their structure along **c**, but whereas β -Si₃N₄ adopts an AAA layering motif, α -Si₃N₄ adopts an A $\bar{A}\bar{A}$ motif that effectively doubles the *c*-axis (Grün, 1979).

Fundamentally there is very little difference in structure between the non-centrosymmetric $P6_3$ and centrosymmetric $P6_3/m$ Si₃N₄ structures. The differences lie only in the presence or absence of the *m* symmetry element normal to the hexagonal *c*-axis. In the centrosymmetric structure all three independent atoms exist on those planes. Breaking of that symmetry element in the non-centrosymmetric case permits minor differential shifts of atom positions along the *c*-axis and leads to subtle changes in the nearest-neighbour bond lengths and angles (Grün, 1979). Bando (1983) suggested that small deviations from the centrosymmetric structure in bulk β -Si₃N₄ arise from the relatively weakly scattering N-atom contributions. Here the term 'bulk' is used to refer to the interior of a pure crystal, free from surface strains. In addition to, or instead of, purely static displacive shifts, anisotropic vibrational motion could also contribute to such symmetry breaking.

The objective of the current work was to use high-precision single-crystal structural studies to resolve the issue in bulk β -Si₃N₄. If structural non-centrosymmetry was really a property of the bulk, this seemed a reasonable approach to identify it. To this end synchrotron X-ray diffraction-based charge-density imaging experiments were undertaken at several different temperatures.

2. Experimental

Crystals of β -Si₃N₄ were prepared from a pure silicon melt at 1900 K under a nitrogen atmosphere and in a silicon nitride crucible, as described by Furuya *et al.* (1999). Millimetre-long,

needle-like filaments of pure β -Si₃N₄ were recovered from the silicon melt. These were crushed, with some difficulty, to find smaller single-crystal fragments suitable for study by synchrotron X-ray diffraction.

Data were measured for two separate crystals on two different occasions using the Diff14A software (Vaalsta & Hester, 1997) to drive a horizontal-type Rigaku four-circle diffractometer mounted on BL14A (Satow & Iitaka, 1989) of the Photon Factory synchrotron, Tsukuba. Before each experiment the wavelength was calibrated using a spherically ground standard Si crystal. An eight-channel avalanche photodiode detector was used for photon counting (Kishimoto *et al.*, 1998). Data were measured for crystal 1 at 295 K. The initial promising results dictated two further experiments at 150 and 200 K to help assess reliability. An Oxford Systems liquid-nitrogen cryostat was used and a minor degree of ice formation was observed only in the 150 K experiment. The 0.7 Å wavelength chosen for the experiments optimizes the available photon flux against the resolution.

Lattice parameters determined in each experiment are recorded in Table 1,¹ along with similar parameters from other experiments and theory-based structural relaxation studies. The lattice parameters determined herein exhibit a smaller variance, even across different temperatures, compared with those of other studies. This implies consistency and higher precision, although not necessarily better accuracy.

Crystal 1 had a shape reasonably approximated by a sphere of radius 0.037 mm. A second smaller crystal was used for the low-temperature experiments and was more plate-like, being 0.018 mm thick, with two large (010) faces. Shape-dependent correction factors ($\mu = 1.53$ mm⁻¹) were applied assuming the atomic absorption attenuation coefficients from Sasaki (1990).

For each experiment, complete spheres of data were measured to enhance the statistics. The 200 K data set also benefited from increased background-counting statistics and a slightly higher resolution. Some high χ angle data, typically two reflections per group of equivalents, were systematically weak, presumably owing to some residual mis-centring of the crystal. Those reflections were removed from the data based on differences of $|I - \bar{I}| > 6\sigma(I)$. All the initial data treatment, up to and including the spherical-atom refinements, was performed using the *Xtal* System (Hall *et al.*, 2003) with the preliminary details of each experiment listed in Table 2.

The structural assessment undertaken below resembles in part that adopted by Abrahams *et al.* (1998) in examining the symmetry of Sr₅Nb₅O₁₇, but here only a subset of their 14 diffraction data tests were undertaken. However, our general approach to data measurement and treatment does reflect the general recommendations of those authors.

3. Data analysis

A simple method for discriminating between centrosymmetric and non-centrosymmetric models that is often used in small

¹ Supplementary data for this paper are available from the IUCr electronic archives (Reference: AV5009). Services for accessing these data are described at the back of the journal.

Table 4

Distributions of normalized structure factors and comparison with estimates based on random centrosymmetric and non-centrosymmetric structures.

$ E > (\%)$	0.00	1.00	1.20	1.40	1.60	1.80	2.00	2.50	3.00
Random $P\bar{1}$	100.00	31.73	23.01	16.15	10.96	7.19	4.55	1.24	0.27
295 K	100.00	35.52	24.70	17.42	9.98	6.14	3.63	0.70	0.00
200 K	100.00	34.58	24.86	17.82	10.48	6.29	3.82	0.57	0.00
150 K	100.00	35.04	24.92	18.08	10.03	6.06	3.55	0.64	0.00
Random $P1$	100.00	36.79	23.69	14.09	7.73	3.92	1.83	0.19	0.01

molecule structural solution procedures is to compare the observed distribution of normalized structure factors with estimates assuming randomly distributed atoms in centrosymmetric or non-centrosymmetric symmetries. Table 3 shows the observed and expected mean values from random estimates while Table 4 shows the distribution of such normalized structure factors with scattering angle. In both tables the experimental values lie midway between the theoretical $P\bar{1}$ and $P1$ symmetry values making this test indecisive.

The Report of the IUCr Subcommittee on Statistical Descriptors (Schwarzenbach *et al.*, 1989) suggests that to discriminate between enantiomorphic models in the least-squares processes one parameter describing the absolute configuration should be refined, whose value and standard uncertainty act as desiderata. The Flack (1983) absolute structure parameter is determined by minimizing a residual based on the differences between $F(h, k, l)$ and $F(\bar{h}, \bar{k}, \bar{l})$ for F_{obs} and F_{calc} , differences which arise from the complex component of the dispersion correction. At 0.7 Å, the X-ray wavelength used here, the complex dispersion coefficients for both Si ($f'' = 0.079$ e per atom) and N ($f'' = 0.04$ e per atom) are rather small (Sasaki, 1989). As a result the relatively minor deviations expected from the broken mirror symmetry result in calculated Friedel-pair structure-factor differences of the order 0.04 e per atom as a maximum with most below 0.005 e per atom. These differences are much smaller than the accuracy of the measured structure factors. It is therefore not surprising that in each non-centrosymmetric structural refinement the Flack parameter converged to a value of $x(u) = 0.5$ (5). Flack & Bernardinelli (2000) point out that an uncertainty as large as $u = 0.5$ indicates simply that the anomalous dispersion is incapable of resolving the absolute configuration and the value of x is therefore unreliable, providing no further information.

To pursue the symmetry issue further, complete structural refinements in both space groups at each temperature were examined. The details of these independent-atom model (IAM) refinements (distinct from the generalized multipolar structure-factor GSF models which follow) are shown in Table 5. Structure factors were calculated from neutral-atom form factors. For each data set the least-squares structural refinement of the lower symmetry structure involves an additional six parameters and consistently leads to a slightly lower R -factor, weighted R -factor and goodness-of-fit. Of the three experiments, the 200 K data has slightly higher resolution, did not suffer from ice formation and has the lowest R -factor. It is therefore favoured here as the most accurate of the three experiments.

Hamilton (1965) showed that the ratio between least-squares R -factors could be used to establish some degree of confidence in one of two linearly related models which fit the same data. To apply his R -factor significance test we formulate the null hypothesis, H_0 : that there is no difference between the high- and low-symmetry configurations, *i.e.* $z(\text{N1}) = z(\text{N2}) = z(\text{Si}) = 0.25$ and $U^{13}(\text{Si}) = U^{23}(\text{Si}) = U^{13}(\text{N1}) = U^{23}(\text{N1}) = 0$. This is a linear hypothesis of dimension 6 (or 7 except that here z was fixed for Si), this being the reduction in the number of free variables, with more than 700 degrees of freedom (reflection number less refined variables). In each experiment the calculated $R_{b,n-m}$ value exceeds Hamilton's $R_{b,n-m,\alpha}$ at the $\alpha = 0.5\%$ significance level meaning that, in principle, there is a more than a 99.5% likelihood that the high-symmetry hypothesis is false.

An alternative checking procedure also suggested by Hamilton (1965) involves using the weighted sum of least-squares residuals in a direct comparison with the F distribution for a given significance level. Draper & Smith (1981) use a more conservative variant, whereby the null hypothesis is rejected only when the experimentally determined F value exceeds the corresponding significance level by a factor of four. Such an approach was adopted by Streltsov *et al.* (1993) in checking the significance of the additional multipolar parameters in studies of LiFePO_4 . According to Draper & Smith (1981), at the 5% significance level the calculated $F_{b,n-m}$ value is less than four times $F_{b,n-m,\alpha=0.05}$ for the 150 K data and the high-symmetry model is useful practically. Alternatively, there is just a 5% likelihood that if the high-symmetry model was rejected, it was rejected in error. In contrast, the large 200 and 295 K $F_{b,n-m}$ values imply almost 100% confidence in the low-symmetry models.

Despite this strong support for the low-symmetry models, it might still be argued that the implicit assumptions of linearity between the free variables and the degrees of freedom are inappropriate, leading to an invalid application of the analysis of variance (ANOVA) methods. Abrahams *et al.* (1998, and references therein) indicate that as the data-to-parameter ratio becomes higher, the test becomes misleading. In addition, the current results are strongly dependent on the values of χ^2 or the goodness-of-fit, which is in turn strongly influenced by the choice of weighting scheme. Refining the weighting scheme would add further parameters to the mix and Abrahams *et al.* (1998) suggest several advantages in avoiding such an approach.

The structural refinements presented here included a Zachariasen (1967) isotropic extinction model. In each of the 150 and 200 K refinements the maximum attenuation by

Table 5
IAM refinement indices, fractional atomic coordinates and anisotropic displacement parameters ($U \times 10^5 \text{ \AA}^2$) for $\beta\text{-Si}_3\text{N}_4$.

$$T = \exp[-2\pi^2(a^{*2}h^2U^{11} + b^{*2}k^2U^{22} + c^{*2}l^2U^{33} + 2a^*b^*hkU^{12} + 2a^*c^*hlU^{13} + 2b^*c^*klU^{23})].$$

	150 K $P6_3/m$	200 K $P6_3/m$	295 K $P6_3/m$	150 K $P6_3$	200 K $P6_3$	295 K $P6_3$	293 K ^a $P6_3$	295 K ^b $P6_3$	0 K ^c $P6_3$
No. of reflections	796	866	796	796	866	796			
No. of variables	16	16	16	22	21	22			
S	1.84 (4)	1.88 (5)	2.01 (5)	1.79 (4)	1.76 (4)	1.88 (5)			
R	0.01426	0.01364	0.01958	0.01395	0.01292	0.01838			
wR	0.01363	0.01142	0.01457	0.01324	0.01062	0.01351			
$n - m$	780	850	779	774	845	774			
$R_{b,n-m}$				1.022	1.056	1.065			
$R_{b,n-m,\alpha=0.005}$				1.012	1.011	1.012			
χ^2	2640	3004	3147	2480	2617	2735			
$F_{b,n-m}$				8.36	24.97	19.60			
$4 \times F_{b,n-m,\alpha=0.05}$				8.44	8.437	8.44			
$4 \times F_{b,n-m,\alpha=0.01}$				11.3	11.29	11.3			
$4 \times F_{b,n-m,\alpha=0.005}$				12.47	12.47	12.47			
r^*	2100 (350)	1296 (440)	1587 (200)	1700 (300)	1600†	2100 (400)			
y_{min} (002)	0.97	0.98	0.94	0.98	0.97	0.95			
$\Delta\rho_{min}$	−0.40 (4)	−0.37 (3)	−0.53 (6)	−0.39 (4)	−0.34 (4)	−0.48 (5)			
$\Delta\rho_{max}$	0.51 (4)	0.45 (3)	0.61 (6)	0.44 (4)	0.37 (4)	0.53 (5)			
Si									
x	0.76848 (1)	0.76848 (1)	0.76848 (2)	0.76847 (1)	0.76848 (1)	0.76847 (2)	0.7686 (1)	0.7686 (1)	0.7663
y	0.17456 (1)	0.17457 (1)	0.17456 (2)	0.17455 (1)	0.17458 (1)	0.17455 (2)	0.1744 (1)	0.1749 (1)	0.1737
z			1/4	C	C	C	C		
U^{11}	272 (3)	313 (2)	312 (3)	272 (3)	298 (2)	316 (3)	672 (30)		
U^{22}	255 (3)	294 (2)	284 (3)	256 (3)	279 (2)	289 (3)	672 (30)		
U^{33}	211 (3)	243 (3)	270 (3)	213 (3)	230 (2)	278 (3)	376 (30)		
U^{12}	127 (2)	146 (2)	139 (3)	127 (2)	138 (1)	142 (2)	351 (30)		
U^{13}				−29 (13)	9 (11)	135 (11)	−67 (100)		
U^{23}				−45 (13)	6 (11)	108 (11)	−134 (100)		
N1									
x	0.03050 (3)	0.03049 (2)	0.03050 (4)	0.03050 (3)	0.03051 (2)	0.03055 (4)	0.0298 (3)	0.0313 (3)	0.0271
y	0.33025 (3)	0.33026 (3)	0.33024 (4)	0.33022 (4)	0.33030 (3)	0.33028 (5)	0.3294 (3)	0.3284 (3)	0.3337
z			1/4	0.2468 (4)	0.2485 (4)	0.2487 (6)	0.2628 (20)	0.287 (2)	0.2726
U^{11}	293 (5)	322 (4)	312 (7)	290 (5)	307 (4)	311 (6)	789 (90)		
U^{22}	444 (5)	502 (4)	548 (7)	444 (5)	486 (4)	553 (7)	760 (90)		
U^{33}	259 (5)	283 (5)	297 (7)	260 (6)	277 (4)	304 (7)	435 (90)		
U^{12}	139 (4)	153 (3)	153 (6)	138 (4)	146 (3)	151 (6)	321 (60)		
U^{13}				0 (30)	−10 (20)	−110 (30)	−402 (300)		
U^{23}				80 (30)	−80 (20)	−70 (30)	−413 (200)		
$\delta z/(U^{33})^{1/2}$ (%)				−18	−8	−7	50		
N2									
x			1/3			1/3			
y			2/3			2/3			
z			1/4	0.2494 (12)	0.2469 (9)	0.2515 (11)	0.2392 (55)	0.237 (5)	0.2353
U^{11}	306 (5)	342 (4)	332 (7)	307 (5)	324 (4)	334 (7)	847 (90)		
U^{22}			U^{11}						
U^{33}	415 (9)	464 (8)	530 (12)	418 (9)	449 (9)	534 (12)	538 (170)		
U^{12}			$U^{11}/2$			$U^{11}/2$	438 (60)		
U^{13}									
U^{23}									
$\delta z/(U^{33})^{1/2}$ (%)				−3	−13	6	40		

References: (a) Grün (1979); (b) Schneider *et al.* (1994); (c) Ching, Ouyang & Gale (2000). † r^* was fixed to this value to ensure a y_{min} value consistent with the other crystal (2) refinements.

extinction was 3%, with the exception of the 200 K $P6_3$ model where it was 5%. As the same crystal was employed at both temperatures and the same data were being treated, we fixed the extinction parameter at a smaller value in accordance with the other results. For the 295 K data the crystal used was around ten times larger in volume and the refinement converged to a maximum 6% correction in both symmetry models, which does not seem unreasonable.

Table 5 shows that for two different crystals across three different temperatures in both symmetries there are no significant differences in the x or y coordinates of any of the atoms. This suggests very good experimental stability. The $P6_3/m$ unconstrained U^{ij} atomic displacement parameters (ADPs) reported in Table 5 also agree well with the matching parameters of the $P6_3$ refinements at the same temperature. The magnitudes of the U^{ij} elements for the two crystal 2 data

sets increase with temperature as might be expected, but the variations are much less systematic at 295 K. However, there are general trends toward larger ADPs along the *c*-axis with reduced vibrational motion in the orthogonal plane at 295 K.

The U^{33} components of Si and N1 are less than or equal to the U^{11} and U^{22} components of the same atoms, and the magnitudes of those components are relatively small. This reflects low uncertainty in their associated atomic positions, along *c*, normal to the possible mirror plane. It also suggests the absence of a broad or multi-modal potential surface, with the consequence that at least for N1 and Si a 1:1 inversion-related twin model seems unlikely. On the other hand, the U^{33} component of N2 is around 1/3 larger than the other principle components. This is still relatively small and quite consistent with the N2 atom's planar bonding geometry. With only three short (~ 1.735 Å) N2—Si bonds in the *x*—*y* plane there are no restrictions on the off-plane displacements of the N2 atom, apart from two unit-cell-translated 2.9 Å contacts with two other N2 atoms along *c*. However, as will be seen in the discussion of the GSF refinements to follow, the model restrictions of an IAM refinement may have misleadingly enhanced the U^{33} component for N2.

Differences between the $P6_3/m$ and $P6_3$ refinement models arise predominantly in the *z* coordinate of N1 and N2, but also from the U^{13} and U^{23} components of Si and N1. In the $P6_3$ refinements reported here, we constrained the *z* coordinate of Si to 1/4 in each case, as an aid for structural comparison. Bando (1983) suggested that possible symmetry breaking involves the rotation of the SiN_4 tetrahedra about an Si axis in the pseudo-mirror planes. This mechanism implies that one or other of N1 or N2 should have $z < 1/4$, while the other should have $z > 1/4$. This conflicts with the 200 and 150 K results, but seems to apply for the data of Grün (included here in Table 5) as well as for our 295 K data. The different senses of rotation for the two N atoms suggest inversion-related crystals although the displacements are much less dramatic for our data.

From the 150 K data the N1 atom is displaced from the $z = 1/4$ plane by -0.0093 (12) Å, while the N2 atom is displaced by -0.002 (2) Å. The N2 atom has a $U^{33} = 0.00418$ (9) Å² ADP component corresponding to an RMS (root mean-square) displacement of ± 0.0647 (5) Å. Consequently the observed mean displacement is $\sim 3\%$ of the RMS ADPs or 1.5% of the RMS range, the significance of which seems rather questionable. N1 on the other hand is displaced by $\sim 20\%$ of its U^{33} RMS value [0.0510 (2) Å], which may well be significant but was not reproducible.

At 200 K both N1 and N2 are displaced below the *m*-plane, by just 8 and 13% of their RMS values, and at 295 K those relative displacements are smaller at 7 and 6%, respectively, although in opposing directions.

Although the 200 K experiment has a better data–model agreement, the 150 K atomic positions show an approximate 15% reduction in ADP amplitudes, which should emphasize the harmonic mean more strongly. Unfortunately, the broad variation with temperature, the limited number of data points and the clustering of those displacements reasonably close to

0% precludes any systematic judgements of temperature dependence.

Other parameters with potentially meaningful information are the non-zero U^{13} and U^{23} atomic displacement parameters for Si and N1, which break the *m* symmetry element. For the 150 and 200 K data sets, these parameters are essentially zero to within four standard uncertainties (s.u.'s), but by 295 K some of those displacement parameters have changed sign, presumably in correlation with the atomic positions. So, even though the latter values are reported here as non-zero by more than 10 s.u.'s, the consistency of those results across the three experiments suggests a much lower significance than the diagonal terms of the least-squares correlation matrix imply. In addition, the signs and magnitudes of the transformed atomic displacement parameters of Grün (1979) determined at 293 K do not bear much resemblance to our 295 K data in absolute terms, although all such symmetry-breaking U^{ij} terms are zero to within 2 s.u.'s.

The small magnitude of the atomic shifts with respect to the mean-square displacement parameters suggests that thermal activation of transitions between two possible enantiomorphic polarities is inevitable. We could therefore expect to find microtwinning with a 1:1 ratio and in such a case the mean atomic potentials should be bimodal. However, by adopting a single moded refinement model in the low-symmetry setting, preferential selection of one mode ought to be accompanied by an increased U^{33} parameter with respect to the mirror symmetry setting. That would compensate for the other unoccupied mode. In fact no significant differences exist in the U^{33} ADP components of any atom, between the two symmetry settings.

4. Geometrical analysis

Bond lengths and angles were calculated from the IAM coordinates and are shown in Tables 6 and 7. Although full least-squares covariance terms were not used in the standard uncertainty calculations, trends across three data sets may provide an added sense of precision.

Each N atom is bonded to three neighbouring Si atoms. For N1 in the $P6_3$ setting there are three unique N1—Si bonds, whereas in the $P6_3/m$ setting those bonds are arranged as a single bond in the plane of the mirror with two mirror-related bonds extending above and below the mirror. For N2 all three bonds are equivalent by threefold symmetry. Consequently, there are three and four distinct Si—N bonds in the $P6_3/m$ and $P6_3$ symmetries, respectively.

Given the equivalence of the three N2 bonds, the near equality of the two independent N1—Si bond lengths in the higher symmetry setting is not unreasonable. There is a uniform 0.005 Å difference between the N1 and N2 bond lengths in each of the high-symmetry models. This suggests a distinct chemical difference between these two inequivalent N sites. In the low-symmetry models the N1—Si bond lengths are also on average about 0.006 Å longer than the N2—Si bonds, but at 200 and 295 K these bond lengths are spread over a 0.007 Å range, which is doubled to 0.016 Å at 150 K. There

Table 6

Temperature- and symmetry-model-dependent bond lengths (Å) from IAM refinements.

	150 K <i>P</i> _{6₃/m}	200 K <i>P</i> _{6₃/m}	295 K <i>P</i> _{6₃/m}	150 K <i>P</i> _{6₃}	200 K <i>P</i> _{6₃}	295 K <i>P</i> _{6₃}
N1—Si	1.7352 (2) 1.73538 (13) ×2	1.73506 (18) 1.73544 (10) ×2	1.7357 (3) 1.73567 (16) ×2	1.7353 (2) 1.7431 (11) 1.7276 (11)	1.73517 (18) 1.7390 (10) 1.7319 (10)	1.7361 (3) 1.7387 (14) 1.7323 (14)
⟨N1—Si⟩	1.7353	1.7353	1.7357	1.7353	1.7354	1.7357
N1—Si range				0.0155	0.0071	0.0064
N2—Si	1.72918 (9) ×3	1.72901 (8) ×3	1.72976 (10) ×3	1.72920 (9) ×3	1.72897 (8) ×3	1.72974 (10) ×3
Si—N2	1.72918 (9)	1.72901 (8)	1.72976 (10)	1.72920 (9)	1.72897 (8)	1.72974 (10)
Si—N1	1.7352 (2)	1.73506 (18)	1.7357 (3)	1.7353 (2)	1.73517 (18)	1.7361 (3)
Si—N1	1.73538 (13) ×2	1.73544 (10) ×2	1.73567 (16) ×2	1.7431 (11) 1.7276 (11)	1.7390 (10) 1.7319 (10)	1.7387 (14) 1.7323 (14)

Table 7

Experimentally determined bond angles (°) from the various IAM refinements.

	150 K <i>P</i> _{6₃/m}	200 K <i>P</i> _{6₃/m}	295 K <i>P</i> _{6₃/m}	150 K <i>P</i> _{6₃}	200 K <i>P</i> _{6₃}	295 K <i>P</i> _{6₃}
Si—N1—Si	123.033 (7) ×2	123.032 (5) ×2	123.038 (8) ×2	123.50 (7) 122.56 (7)	123.25 (6) 122.82 (6)	123.22 (8) 122.83 (8)
	113.708 (10)	113.708 (10)	113.697 (15)	113.709 (10)	113.710 (9)	113.716 (15)
Si—N2—Si	120 ×3			119.997 (5)	119.997 (5)	119.999 (4)
N2—Si—N1	106.601 (11)	106.600 (9)	106.602 (13)	106.605 (11)	106.599 (9)	106.601 (14)
N2—Si—N1	110.098 (10) ×2	110.096 (8) ×2	110.103 (13) ×2	109.96 (10)	109.78 (8)	110.19 (10)
N2—Si—N1				110.25 (10)	110.40 (8)	110.00 (10)
N1—Si—N1	108.023 (9) ×2	108.026 (8) ×2	108.024 (12) ×2	107.66 (4)	107.87 (4)	107.88 (5)
N1—Si—N1				108.36 (4)	108.19 (4)	108.17 (5)
N1—Si—N1	113.708 (10)	113.708 (8)	113.697 (12)	113.71 (3)	113.71 (3)	113.72 (4)

was no measurably significant temperature dependence of the mean N—Si bond lengths. Although there is an increase of 0.0007 (2) Å for N2—Si between low and room temperature, this is within 4 s.u.'s. Perhaps this stability is not overly surprising given the refractory nature of the compound.

Grün (1979) argued that because the N1Si₃ groups are non-coplanar, it would be incongruous if the N2—Si bonds were so constrained. The argument was supported by the α -Si₃N₄ structure of Kato *et al.* (1975) for which the four independent N atoms all exhibit non-planarity to varying extents. However, this ignores the relative differences in bond lengths, which for the α phase are typically longer than 1.740 Å, and for N1 and N2 are around 1.735 and 1.729 Å, respectively. The N2 atom bonds are shortest and trigonally symmetric, so it is not unreasonable for the constraints of *sp*² hybridization symmetry to be correspondingly stronger, limiting such N2 atom off-planar shifts to values below that observed for N1.

For triply coordinated NX₃ molecular structures such as NH₃, the strongly localized N-atom lone-pair electrons act to repel the electrons involved in bonding. This deforms the ideally trigonal planar *sp*² configuration towards a tetrahedral *sp*³-like conformation, with 109.18 (5)° bond angles for NH₃ (Boese *et al.*, 1997). For lattice-type compounds the electrostatic crystal field is not inconsiderable and it could well act to reinforce the spatial symmetry of the lattice, suppressing any tendencies toward tetrahedral distortion, especially along high-symmetry axes.

The off-planar displacements of N2 vary from 0.004 to 0.027 Å and for N1 are relatively stable at 0.048 Å for both

symmetries and at three temperatures (and in excellent agreement with Grün, 1979). Deviations from coplanarity in *P*_{6₃} could also affect the Si—N2—Si bond angles, but they remain ideal to within 1 s.u. For N1 the broken symmetry allows an extra 0.5° variation in the bond angles, or about an extra 15% on the distortions already present in the *P*_{6₃/m} model. For the Si atom the deviations from ideal tetrahedral (109.47°) bond angles in *P*_{6₃/m} symmetry is up to 4.25°, with an additional 10% arising with the broken mirror.

The largest deviations in the forgoing discussion arise for the low-symmetry 150 K data and depend strongly on the larger off-plane displacement of the N1 atom. For the 200 and 295 K data, low-symmetry variations were *ca* 1/2 to 1/3 less than the 150 K results. If the 150 K results are temporarily excluded, it appears that symmetry breaking leads to only 5% variations in bond lengths and angles beyond those already present in the high-symmetry structure.

5. Time-averaged dynamical electron density

In high-precision X-ray diffraction experiments the reproducibility of the deformation electron density [$\Delta\rho(\mathbf{r})$] between different experiments, as well as the internal consistencies of charge-density features within each experiment, provide additional checks for reliability. Here we are talking about differences between the measured and independent atom (IAM) or procystal densities.

Although the symmetry and structure of β -Si₃N₄ is reasonably complex, $\Delta\rho(\mathbf{r})$ along all the primary N—Si

interaction vectors is adequately represented by just two contour maps, each centred on a unique N atom and containing their three respective (virtually) coplanar N—Si

bond vectors. $\Delta\rho(\mathbf{r})$ maps determined at three temperatures and in two symmetry models are presented here in Figs. 2 and 3 for atoms N1 and N2, respectively.

The N1 nuclei are displaced very slightly from the planes of Fig. 2, as indicated therein. Quick checking shows that the $\Delta\rho(\mathbf{r})$ topographies around both N1 and N2 have very similar character in each experiment, thereby establishing the reproducibility and reliability of the experiments.

Around both independent N atoms there is significant accumulation of charge density along the Si—N bonds, maximizing toward the bond midpoints. In Fig. 3 the threefold symmetry around N2 helps to accentuate this feature, whereas the lower N1 site symmetry in Fig. 2 reflects the two independent N1—Si density maxima for the $P6_3/m$ settings (a, c and e), with three independent N1—Si bond maxima in the $P6_3$ setting (b, d and f). Differences in topography between each symmetry model are mostly much smaller than those between data sets and temperatures. In particular, the pseudo- m -symmetry in the $P6_3$ setting shown in Figs. 2(b), (d) and (f) persists quite strongly. This would seem to discredit any conceivable models in which aspherical redistributions of charge density around the nuclei were responsible for breaking the $P6_3/m$ symmetry. However, the apparent $\Delta\rho(\mathbf{r})$ m -symmetry is not sufficient evidence to categorically exclude the broken m -

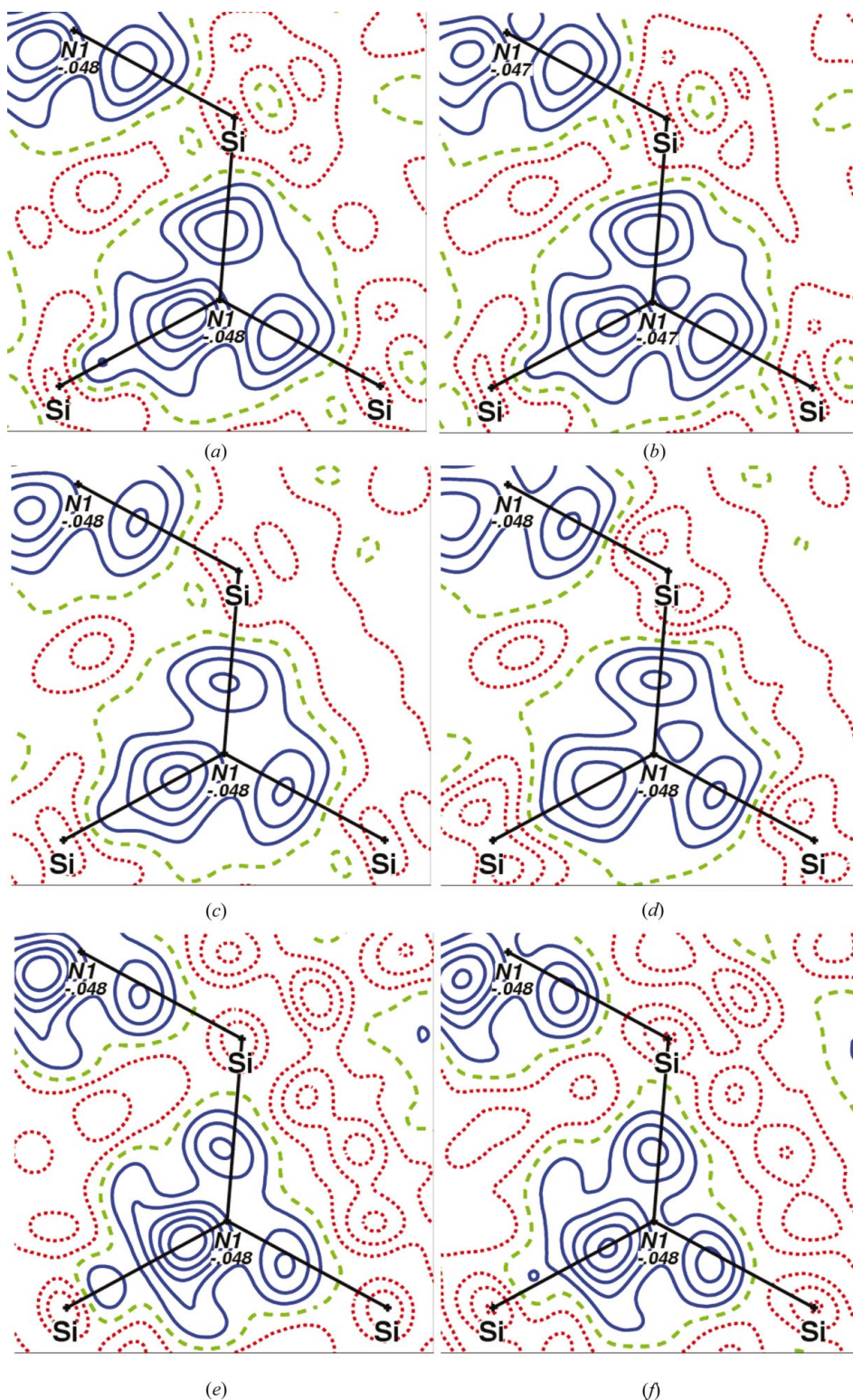


Figure 2

Residual $\Delta\rho(\mathbf{r})$ localized about N1 and calculated with reference to the high-symmetry $P6_3/m$ IAM models at (a) 150, (c) 200 and (e) 295 K, and for the $P6_3$ models at (b) 150, (d) 200 and (f) 295 K. Contours: $0.1 \text{ e } \text{\AA}^{-3}$; positive densities: continuous; negative densities: dotted; zero level: dashed. Map borders: $4.0 \times 4.0 \text{ \AA}^2$.

symmetry of the total density.

In addition to the bond-directed topography, other features of the maps shown in Figs. 2 and 3 are similar across the three experiments. In particular, the broad depleted regions surround the N atoms and extend towards the centres of the

various structural ring systems. Also, the magnitudes of the topographies at the nuclei are very similar, with the Si sites consistently depleted of density with respect to the IAM model, and the N atoms generally located in a slight $\Delta\rho(\mathbf{r})$ excess. This argues in favour of partial charge transfer from Si

to N, with partial ionic bonding complementing the shared electron interactions maximized near the Si–N bond midpoints. Quantitative support for this argument comes from the Hirshfeld (1977) atomic charges presented in Table 10 and determined by the projection of the measured $\Delta\rho(\mathbf{r})$ onto atomic basis functions (Spadaccini, 2000).

Focusing more closely on the bonding density, along the 1.729 Å N2–Si bonds in Fig. 3 the $\Delta\rho(\mathbf{r})$ maxima are consistently $\sim 0.35 \text{ e } \text{\AA}^{-3}$ and located about 0.70 Å from N2. The position is in accordance with the smaller atomic radii of N (0.65 Å) compared with Si (1.11 Å), and also its greater electronegativity. For N1 the $\Delta\rho(\mathbf{r})$ maxima along the two (pseudo) mirror-related Si–N1 bonds are slightly weaker ($0.30 \text{ e } \text{\AA}^{-3}$) and located about 0.64 Å from N1, but within the (pseudo) mirror plane the maxima are stronger ($0.40\text{--}0.50 \text{ e } \text{\AA}^{-3}$) and closer (0.45 \AA) to the N1 nucleus. As there are only modest differences between the N1–Si bond lengths this must reflect the angular asymmetry of the N1 atom's atomic packing. The two mirror-related N1–Si bonds in Figs. 2(a), (c) and (e) form an Si–N1–Si bond angle of just 113° and are presumably squeezed together by lattice strain, forcing the $\Delta\rho(\mathbf{r})$ along those bonds out toward

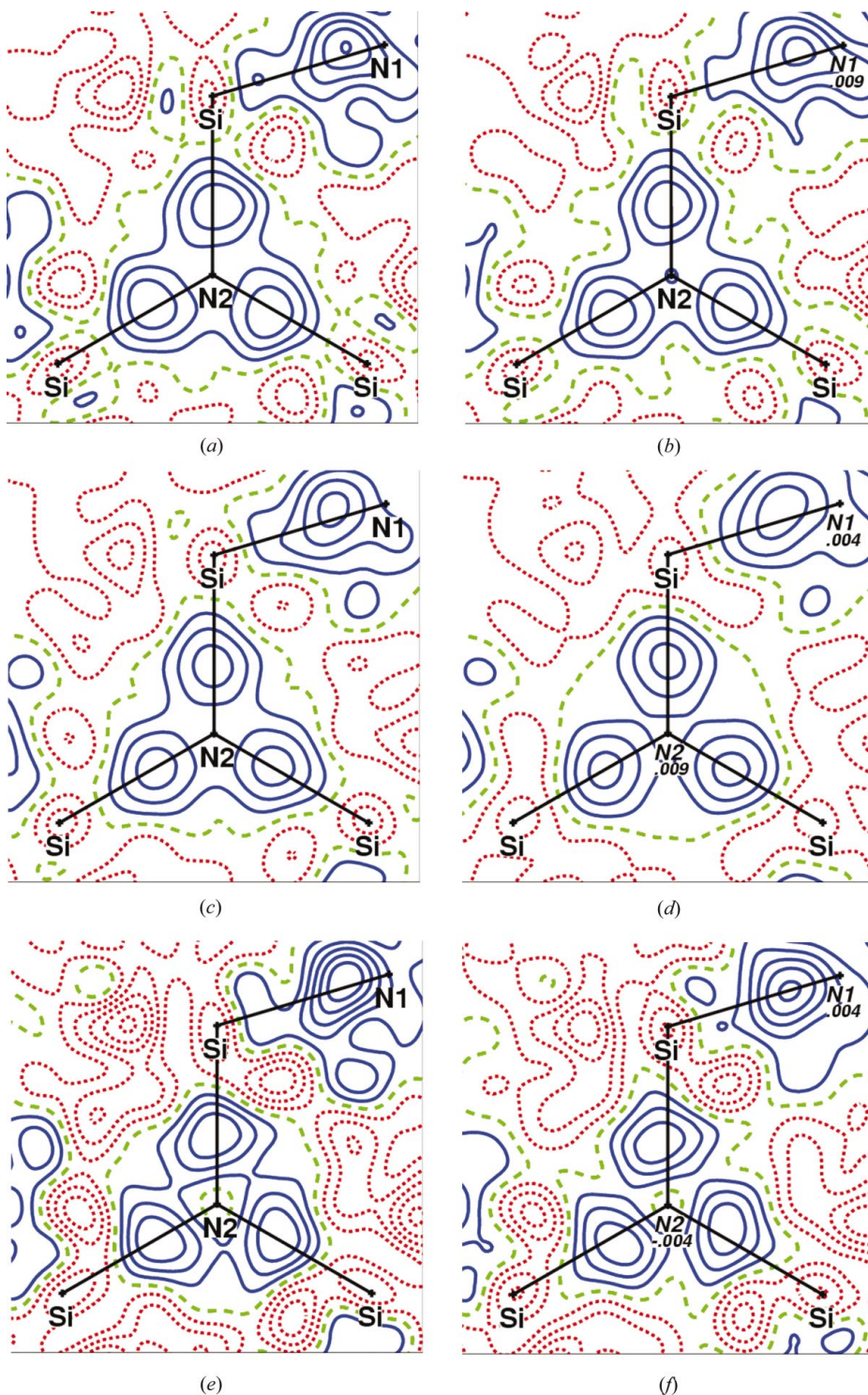


Figure 3

Residual $\Delta\rho(\mathbf{r})$ localized about N2 and calculated with reference to the high-symmetry $P6_3/m$ IAM models at (a) 150, (c) 200 and (e) 295 K, and for the $P6_3$ models at (b) 150, (d) 200 and (f) 295 K. Contours as for Fig. 2.

Table 8

Least-squares refinement details for the β -Si₃N₄ GSF models, including the goodness-of-fit, S , R -factors, fractional atomic coordinates, anisotropic displacement parameters ($U^{ij} \times 10^2 \text{ \AA}^2$), various monopole populations, κ' (dimensionless) and the radial factors α_l (\AA^{-1}).

	150 K	200 K	295 K
Reflections	796	866	796
Variables	96	96	96
S	1.3360	1.4225	1.7369
$R(F)$	0.0101	0.0090	0.0147
$wR(F)$	0.0093	0.0079	0.0114
r^*	0.00079	0.00079	0.00120
Residual $\Delta\rho_{\min}$	−0.24 (2)	−0.26 (2)	−0.30 (2)
Residual $\Delta\rho_{\max}$	0.28 (2)	0.12 (2)	0.34 (2)
Si			
x	0.76850	0.76847	0.76850
y	0.17457	0.17455	0.17454
z	1/4		
U^{11}	0.28925	0.32771	0.39220
U^{22}	0.27073	0.30622	0.35661
U^{33}	0.18185	0.19724	0.32558
U^{12}	0.14001	0.15024	0.17728
Core (e)	2		
Pseudo (e)	8		
Valence (e)	4.0075	4.0336	3.3145
κ'	0.9727	0.9615	1.0691
α_1	4.5046	4.6006	2.7007
α_2	6.5392	6.2355	4.883
α_3	6.3984	6.3207	6.2384
α_4	8.6337	8.5504	8.3605
N1			
x	0.03045	0.03045	0.03033
y	0.33024	0.33001	0.33013
z	1/4		
U^{11}	0.32605	0.34571	0.39992
U^{22}	0.51216	0.56797	0.63659
U^{33}	0.23371	0.26375	0.33005
U^{12}	0.16525	0.15426	0.19691
Core (e)	2		
Valence (e)	4.9943	4.9748	5.5142
κ'	0.9944	0.9959	0.9573
α_1	12.7754	10.3002	9.4554
α_2	5.5474	6.1528	5.548
α_3	8.1881	6.6529	7.0274
α_4	5.6178	5.9524	4.6511
N2			
x	2/3		
y	1/3		
z	1/4		
U^{11}	0.33253	0.39786	0.44785
U^{22}	U^{11}		
U^{33}	0.51352	0.41781	0.67158
U^{12}	$U^{11}/2$		
Core (e)	2		
Valence (e)	4.9943	4.9748	5.5142
κ'	0.987685	0.984238	0.954739
α_1	6.992	6.992	6.992
α_2	6.9538	9.08	9.7948
α_3	5.9118	6.3408	7.6821
α_4	8.8645	8.4497	11.4971

the larger bond angles with slight off-centring of the local maxima along those bond vectors, almost reminiscent of the bent bonds of cyclobutadiene (Coppens, 1998).

6. Multipolar refinements

In view of the insensitivity of the $\Delta\rho(\mathbf{r})$ to the broken mirror and the otherwise chemically relevant information it appeared to contain, the data were reexamined assuming only P_{63}/m

symmetry and in terms of generalized structure-factor (GSF) models. Density-localized (Stewart, 1980) analogues to the ground-state neutral-atom wavefunctions of Clementi & Roetti (1974) were used as bases for modelling the experimental densities around N and Si.

Within VALRAY (Stewart *et al.*, 2000) the atomic densities were partitioned into spherically symmetric cores ρ_{core} , a filled pseudo-core shell for Si, and surrounded by partially filled valence monopoles ρ_{val} . This partitioning permits parameterization of the expansion or contraction (κ' refinement) and population (P_{val}) of ρ_{val} following the model of Hansen & Coppens (1978). The monopole populations provide another estimate of the atomic charges, but here N1 and N2 were constrained to have identical values while varying against Si in order to preserve the charge neutrality.

Whereas the monopole densities are derived from wavefunctions comprised of sums of Slater-type functions ($\sum C_j r_j^{n_j} e^{-\alpha_j r}$), the higher-order poles involve only a single Slater-type function, of maximum amplitude near $r = n_l/\alpha_l$.

Here ρ_{val} was expanded as a multipole series up to hexadecapole order ($l = 4$), refining the monopole population P_{val} , κ' , multipole populations P_l^m and the α_l radial exponents.

$$\rho_{\text{val}} = P_{\text{val}} \sum C_j r_j^{n_j} e^{-\kappa' \alpha_j r} + \sum_{l=1}^4 r^{n_l} e^{-\alpha_l r} \sum_{m=-l}^{m=l} P_l^m p_l^m(\cos \theta) e^{im\varphi}. \quad (1)$$

The integral radial powers n_l in the expansion are arbitrary though constrained to $n_l \geq l$ (Stewart, 1977). Various combinations and optimizations of n_l and α_l have been explored by other authors (Hansen & Coppens, 1978; Spackman, 1986; Spackman *et al.*, 1987; Kirfel *et al.*, 2001). Here for $l = 1..4$, we adopted n_l values of 4468 and 2234 for Si and N, respectively. Some experimentation with alternative choices showed that these gave slightly better fits to the experimental data. The associated parameters α_l were initially set to common values following the experiences of previous authors, but for β -Si₃N₄ the refined values were quite different for each pole order l .

The tetrahedral coordination of Si and the trigonal coordinations of N1 and N2 are all strongly dominated by anti-symmetric octopole terms of the order $l = 3$ (Coppens, 1998). Expansion including terms up to hexadecapole order should therefore be adequate to describe the more diffuse perturbations from such ideal charge-density configurations. The dominant octopole contributions for N1 and N2 are maximized at around 0.45 and 0.47 Å along the Si–N 1.735 Å bonds, while for Si the octopole terms are maximized near 0.94 Å.

The m point-group symmetry restricts the available spherical harmonics for all atoms by around 1/3. For N2 the additional threefold character (actually $\bar{6}$) excludes all dipolar terms and there are only four non-zero contributions up to hexadecapole order.

A further reduction in weighted R -factor by around 10% was obtained including third- and fourth-order cumulants in a Gram–Charlier expansion (Zucker & Schulz, 1982) for all atoms. This considerably improved the agreement between the

experimental and theoretical $\Delta\rho(\mathbf{r})$ densities along the bonding vectors, which became more localized rather than broadly distributed along the length of the bonds.

GSF refinement was carried out in a blockwise manner, commencing with positional and harmonic ADP parameters, followed by both third- and fourth-order cumulants, then kappa and monopole refinement, next the multipole populations and finally high-order multipole radial expansion terms. Two iterations were made through the blocks, followed by a refinement of all parameters collectively. One exception was made for the symmetry-restricted C^{ijk} components of N2, which were refined separately as a semiconstrained block to approximate values before the final refinement of all parameters. At the last cycle all parameter correlations were below 71%. Dispersion corrections were not included because of their small magnitude, and the imprecise manner in which they are estimated and applied (Stewart *et al.*, 2000), as well as their additive 0.006 contribution to the refinement R -factors. Isotropic extinction was refined with the initial scale position

and harmonic parameters and fixed at the refined value thereafter. Relevant refinement details are listed in Table 8.

7. Theoretical calculations

β - Si_3N_4 is a ceramic insulator with a wide band gap, making it an almost trivial case for study by current density-functional theory standards. As all valence electrons are strongly bound, there are no delocalized conduction-band electrons with concomitant needs for exotic treatments of exchange correlation or spin polarization and spin-orbit coupling.

Herein we used the augmented plane-wave (APW) method embodied in *Wien2k* (Schwarz *et al.*, 2001), with electron correlation governed by the generalized gradient approximation (GGA) of Perdew *et al.* (1996). In *Wien2k* the valence electron density is partitioned into non-overlapping spherical regions (muffin tins), expanded in terms of spherical harmonics, with the interatomic density modelled by Bloch waves. Muffin-tin radii of 0.847 Å were used for all atoms and spherical

harmonics, including terms up to the order $l = 8$, were used as a basis set to describe the muffin-tin interiors. The core density was supplemented by additional local orbitals catering for the Si semi-core $2p$ states and N1 and N2 $2s$ states.

Of the order of 6000 plane waves were included subject to $\text{RMT} \cdot k_{\text{max}} = 11$. Evaluation for 1000 k -points in reciprocal space reduces to just 81 irreducible points in the Brillouin zone. Similarly, 50 k points reduce to 8 points, but apart from significant time savings for the latter the calculation results were not perceptibly altered. Although the relativistic effects are increasingly important for more accurate treatment of heavier elements, here we used a non-relativistic calculation. Discrepancies between the core densities of the neutral, spherically symmetric, relativistic Hartree–Fock reference atoms and the optimized APW model were considerably smaller in this case, which made for less

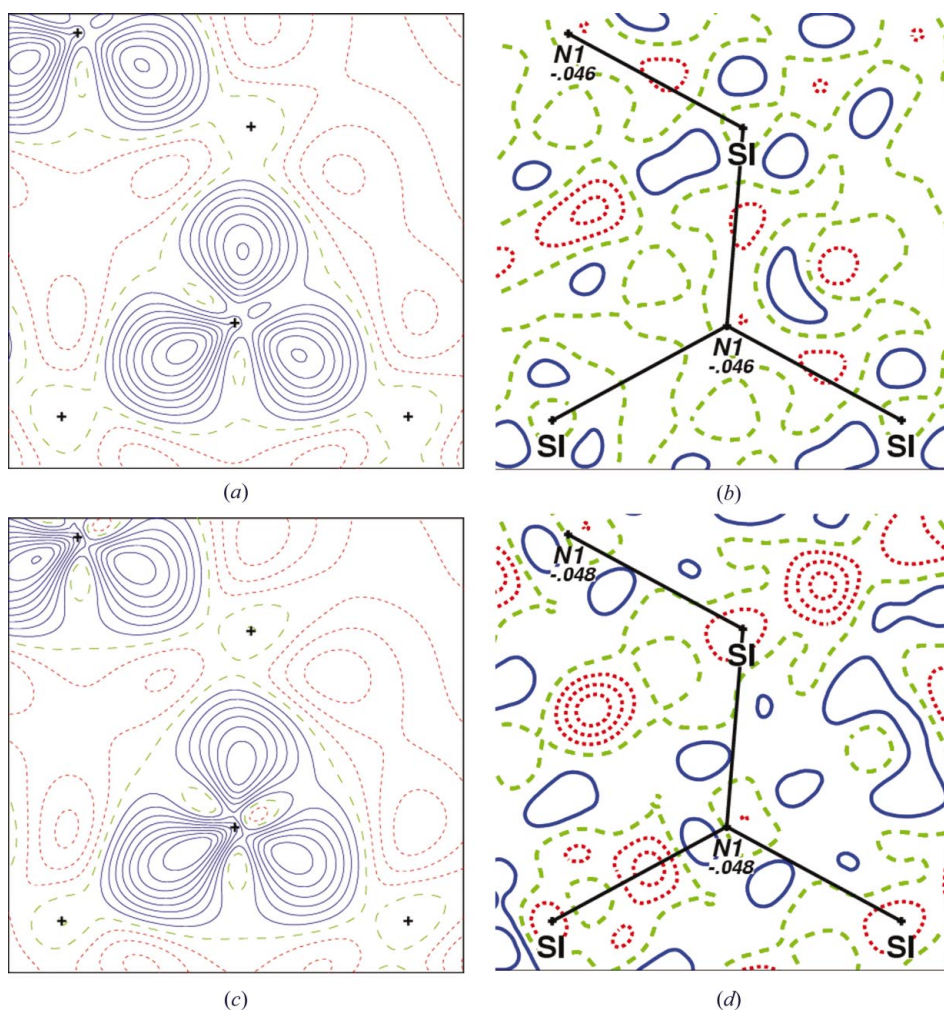


Figure 4

N1 localized $\Delta\rho(\mathbf{r})_{\text{stat}}$ and $\Delta\rho(\mathbf{r})$ determined at (a) and (b) 200 K, and (c) and (d) 150 K, respectively. $\Delta\rho(\mathbf{r})$ is the Fourier transform of the GSF and IAM structure-factor differences, terminated at $\sin \theta/\lambda = 0.90$. All contours: $0.05 \text{ e } \text{\AA}^{-3}$; positive densities: continuous; negative densities: dotted; zero level: dashed. Map borders: $4.0 \times 4.0 \text{ \AA}^2$.

distracting comparisons with the experimental deformation electron density $\Delta\rho(\mathbf{r})_{\text{stat}}$. It is not uncommon for difference densities derived from DFT to vary considerably between different models near the atomic nuclei. Zhuo *et al.* (1997) made extensive comparisons between DFT, experimental charge densities and spherical atom reference models for single-crystal silicon. They found the best agreement using a multiconfigurational Dirac–Fock (MCDF) reference model, but even there residual nuclei-centred differences remain.

The full-potential APW calculations reproduced excellently the character of the band structure reported by Liu & Cohen (1990) and also were in qualitative agreement with the static deformation densities reported by Matsunaga *et al.* (2000) from Hartree Fock molecular orbital calculations of $\text{Si}_3\text{N}_{10}\text{H}_{18}$ clusters.

8. Static deformation electron density

The static deformation electron density $\Delta\rho(\mathbf{r})_{\text{stat}}$ is the difference between the GSF model density and the IAM density, in which both are without any contribution from the

experimental atomic vibrational motion. $\Delta\rho(\mathbf{r})_{\text{stat}}$ is therefore directly comparable to ground-state theoretical densities. Figs. 4 and 5 show the NSi_3 planes for both N1 and N2 at 150 and 200 K, permitting comparison with the DFT analogues shown in Fig. 6. Each experimental map is accompanied by a residual error map of $\Delta\rho(\mathbf{r})$, determined from the experimental and GSF model structure-factor differences for low-angle data truncated at 0.9 \AA^{-1} . For the residual maps the mean error is around 0.01 e \AA^{-3} . The residual densities contain topographical features of magnitude up to 0.2 e \AA^{-3} in the 150 K data. The residuals appear to be distributed in a broadly similar manner for both experiments, suggesting that the GSF model has not captured all of the scattering information present. The 295 K data were considerably noisier and were omitted here.

The static deformation densities in Figs. 4 and 5 again confirm the similarity of the features around N1 and N2. For N2 the $\bar{6}$ symmetry highlights three pronounced N2–Si shared electron interactions, maximizing at between 0.35 and 0.40 e \AA^{-3} , approximately 0.50 \AA from N2. For N1 the two inequivalent bonds have maximal values of $0.30 (\times 2)$ and

between 0.4 to 0.5 e \AA^{-3} , occurring around 0.45 or 0.42 \AA from the N1 nucleus. In each case the bond maxima are closer to the N nuclei than might be expected from the packing of hard spheres with radii 0.75 \AA (N) and 1.1 \AA (Si). This contraction toward N is in good agreement with the electronegativities of N and Si, which are 3.0 and 1.9, respectively. It is also consistent with the higher atomic charges on N determined from the sum of refined monopoles in the three experiments. The magnitudes of the features also compare favourably with those observed along the Si–O bonds [$0.39 (8) \text{ e \AA}^{-3}$] in stishovite (Kirfel *et al.*, 2001) for example.

Although there are certainly differences in $\Delta\rho(\mathbf{r})_{\text{stat}}$ between the experiments, large structural changes are not expected whereas residual random and systematic errors are inevitable. The 150 K results show an increasingly differential polarization along the two independent N1–Si bonds in Fig. 4(c), but that does not correlate with the $P6_3/m$ bond lengths or angles in any appreciable way. The electron density appears more elongated along the single unique N1–Si bond at 150 K than 200 K. It was also more elongated at 295 K so possibly this reflects deficiencies of the model. The larger magnitude of the residual

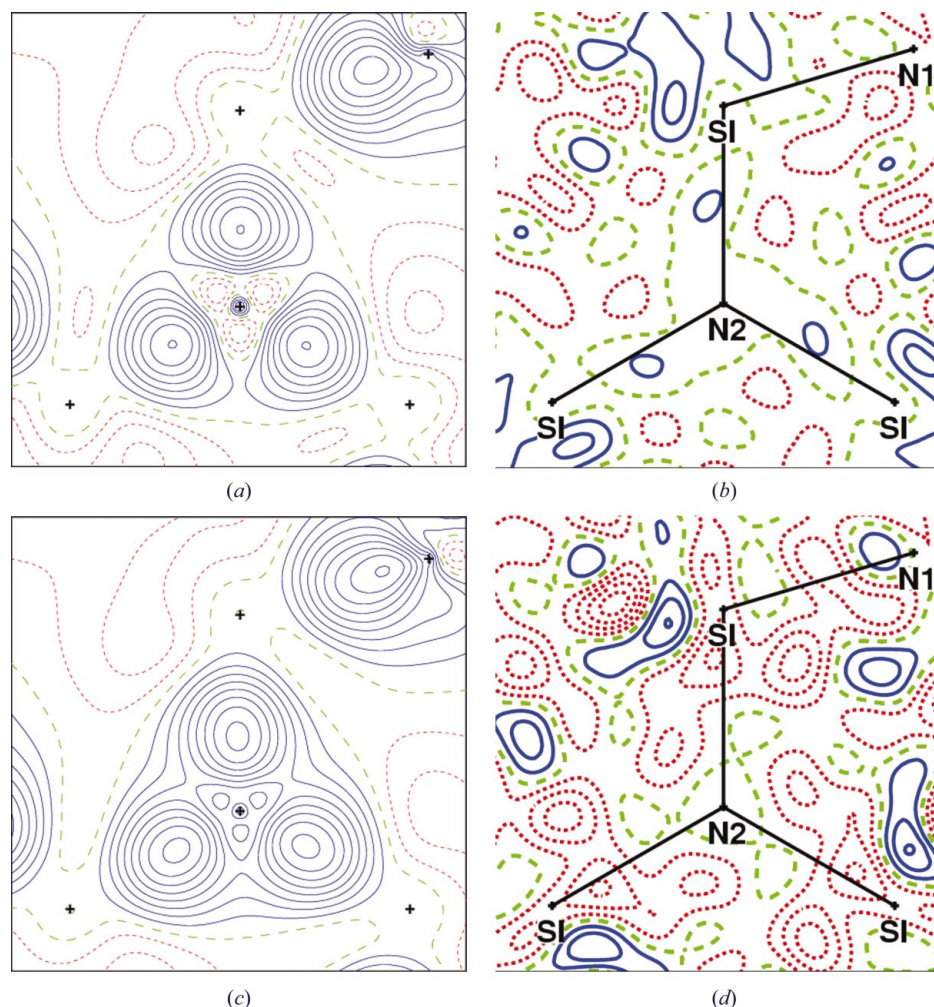


Figure 5
 $\Delta\rho(\mathbf{r})_{\text{stat}}$ multipoles and $\Delta\rho(\mathbf{r})$ residuals for N2. Sources and contours as for Fig. 4.

features of the 150 K maps in Fig. 4(d) and Fig. 5(d) would also tend to support this analysis.

The experimental densities for N1 in Fig. 4(a) and N2 in Fig. 5(a) show very good agreement with the DFT-based densities of Fig. 6. With the exception of the nuclear regions, discrepancies between them involve secondary details, such as the overall morphology of the bonding density which remains more elongated along the bond path in all of the experiments. This could reflect the somewhat contrived radial dependence of the low-order multipoles and the reduced multipole order of the experimental model. Also, the theoretical density in Fig. 6(a) is not as strongly maximized along the unique N1—Si bond as it appears from experiment.

Far more discrepancy is to be found between the 200 K data and DFT shown in Fig. 7. These planes are oriented orthogonal to the sections of Figs. 4 and 5 and, in principle, contain the filled N-atom p_z orbitals normal to the plane of sp^2 bonding. Figs. 7(c) and (d) show clear evidence of such localized density very close to both N-atom nuclei in the DFT calculations. For each atom two density accumulations $0.50 \text{ e } \text{\AA}^{-3}$ in magnitude exist, maximizing around 0.20 \AA from the N atom nuclei. Fig. 7(a) shows that experimentally N1 is quite asymmetric, with a single broad and distorted lobe of $\sim 0.25 \text{ e } \text{\AA}^{-3}$ occurring on one side. Fig. 7(b) shows symmetric, mirror-related accumulations of only $0.20 \text{ e } \text{\AA}^{-3}$ maximized 0.43 \AA from the N2 nucleus.

There are many possible reasons for the localized p_z disparities. It could be that the experimental densities accurately image the real high-temperature modifications of the 0 K DFT results. Alternatively, experimental resolution issues, random and systematic measurement errors, GSF model deficiencies or correlated refinement parameters may be combining to distort the density from true theoretical values. The close proximity of the p_z orbitals to the nuclei in the DFT maps suggests a possible correlation with the harmonic displacement parameters, particularly the large U^{33} compo-

nents typical for N2 and U^{22} for N1. However, in the 200 K GSF refinement the N2 ADPs were very close to isotropic, in contrast to all other refinement results. The N1 ADPs at 200 K remain significantly anisotropic, but in this case the experimental $\Delta\rho(\mathbf{r})$ asymmetry may be coupled with the consistent 0.05 \AA displacement of N1 from its coordination plane. Fig. 7(a) could therefore indicate the onset of a tendency toward tetrahedral sp^3 -like behaviour, driven by lone-pair electron repulsion.

9. Topological analysis

Bader's (1990) theory of atoms in molecules (AIM) relates various properties of a chemical system to the topology of its total electron density. The positions and densities at the critical points where the gradient of the total electron density goes to zero in all directions conveniently represent a great deal of information about the atomic interactions in the lattice.

In the context of chemical interactions, the so-called (3,−1) saddle or bond critical points (b.c.p.) are of most interest, typically arising where the total electron density is minimized along the interatomic bonding vectors. Shared electron interactions such as covalent bonds are often accompanied by strong accumulations of density coincident with the b.c.p. On the other hand, electron-transfer interactions such as ionic bonding lead to much lower electron densities at the b.c.p.

Here the b.c.p.'s were determined from the static GSF modelled density of each experiment as well as from the IAM procrystal and DFT. In the $P6_3/m$ setting of $\beta\text{-Si}_3\text{N}_4$ each of the three distinct Si—N bonding vectors is accompanied by a unique b.c.p., but four b.c.p.'s were detected from the various analyses and are shown here in Table 9. The fourth b.c.p. is manifest at the high-symmetry $\bar{6}$ site midway between the 2.94 \AA N—N contact and has very similar properties in all five topological analyses.

For the other three b.c.p.'s there is very good agreement

between the experimental models, with close but subtle differences with respect to the IAM and DFT analyses. This is in good agreement with the high correspondence between the b.c.p.'s of the procrystal and theoretical densities reported by Downs *et al.* (2002) in their extensive studies of metal–oxygen bonding. Compared with the procrystal, the experimental positions of the Si—N b.c.p.'s are very similar, as also are the principle curvatures λ_3 of the density along the bonds. However, where

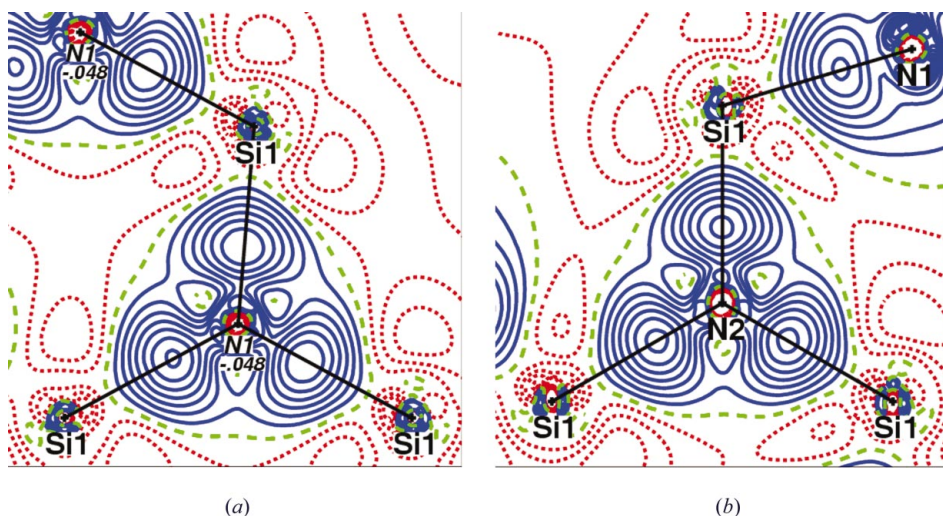


Figure 6

$\Delta\rho(\mathbf{r})_{\text{stat}}$ densities determined from DFT for N1 and N2, assuming a spherical-atom relativistic Hartree–Fock reference model (Desclaux, 1969). Contours and map borders as for Fig. 4.

they differ is in the increased density at the site of the b.c.p. Since the IAM procrystal is purely the superposition of densities of non-interacting atoms, the excess density in the experiments reflects the real drawing-in of density into the bonding region associated with covalent bonding. It is accompanied by larger curvatures, λ_1 and λ_2 , as the density is maximized to a higher value in the tangential plane, and that in turn contributes to their smaller Laplacians [$\nabla^2\rho(\mathbf{r}_c)$] compared with the IAM.

With respect to the experimental results, the DFT Si—N b.c.p.'s are consistently closer to the Si atoms and the principle curvature, λ_3 , along the bond is much sharper, with a lower minimum density $\rho(\mathbf{r}_c)$. Given the experimental scatter amongst the curvatures λ_1 and λ_2 , which are normal to the Si—N bonding vectors, it should not be surprising that the associated b.c.p. ellipticities are also quite broadly distributed. Consequently, there is no consistent agreement with either the DFT or IAM results.

Deviations of the b.c.p.'s from the Si—N bond vectors were insignificant in all of the analyses. The Si—N bonds are

therefore not bent to any appreciable extent, despite the distorted coordination geometry of N1. More importantly, the b.c.p.'s are located more than twice the distance from the N-atom nuclei as the bond-directed covalent $\Delta\rho(\mathbf{r})_{\text{stat}}$ maxima, thereby showing that the formal atomic radii are inappropriate for describing the relative sizes of the bonded Si and N atoms. The Si—N b.c.p. densities $\rho(\mathbf{r}_c)$ are also lower than expected for covalent bonding, which is further evidence of partial ionic bonding, in good agreement with the differing Si and N electronegativities.

Bader's zero-flux surfaces (Bader, 1990) were determined for the three independent atoms of the DFT density and are shown in Fig. 8. The relative volumes of the Si and N attractor basins are quite comparable to those determined for Si and O in stishovite by Kirfel *et al.* (2001), even though the basin shapes themselves differ markedly. The partitioning clearly demonstrates the contraction of the Si atomic basin towards something resembling a small sphere with tetrahedrally disposed fringes, reflecting its coordination environment. The larger N atom basins have corresponding indentations near

the b.c.p.'s where the Si and N basins meet. The N2 basin strongly resembles a triangular prism, while the N1 basin is more irregular and elongated along a pseudo-threefold axis.

Ring critical points (3,+1) were identified at the centres of most of the ring systems. For the distorted, eight-membered (chair conformation) ring system, the centre was actually identified from the midpoint of two slightly offset and symmetry-related critical points. A single cage or (3,+3) critical point was identified, occurring at each of the symmetry-related vertices of the N2 basin triangular prism faces of Fig. 8. It represents the point of intersection of eight separate attractor basins.

An additional ring-critical point was found at the midpoints of the N2 basin's triangular face edges and the fourth b.c.p. arose at the very centre of those faces, midway between pairs of mirror-related N2 atoms. The

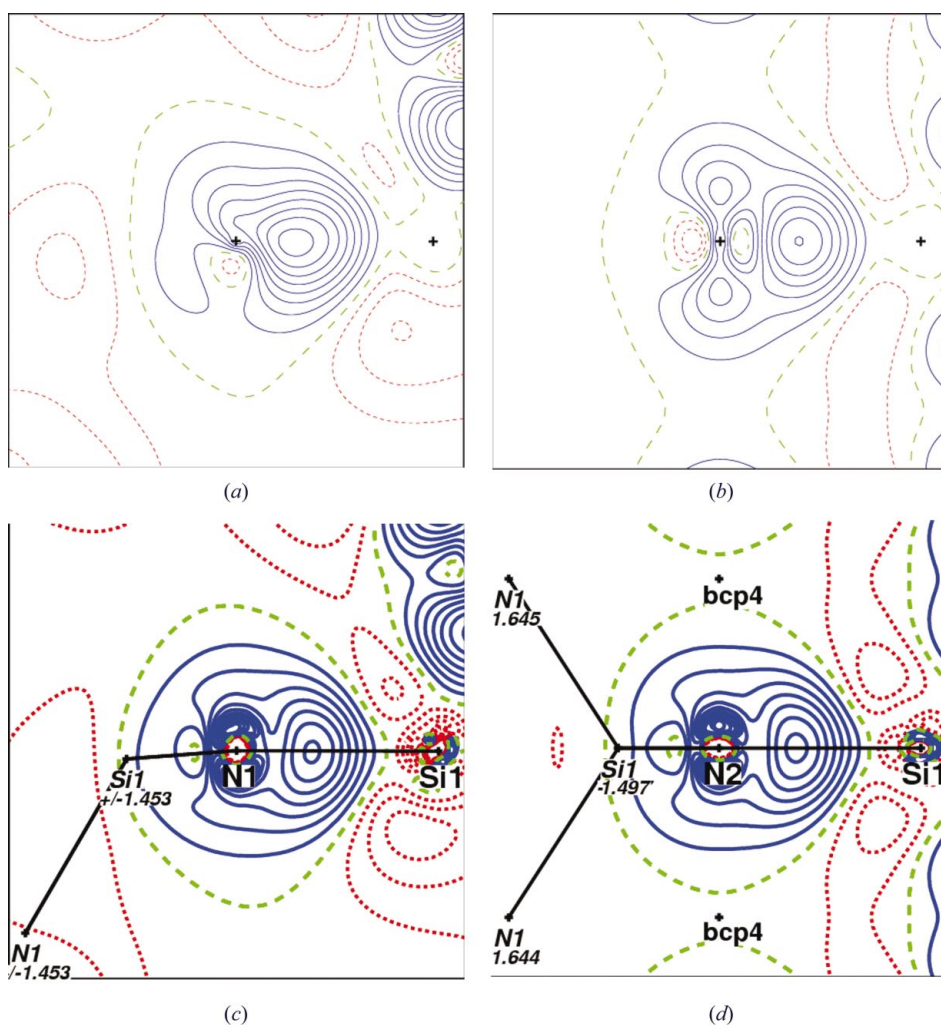


Figure 7

$\Delta\rho(\mathbf{r})_{\text{stat}}$ normal to the bonding planes and containing a single N—Si bond and the filled N atom p_z orbital, for both N1 and N2. Data derived from (a) and (b) the 200 K experiment, and (c) and (d) DFT with contours as for Fig. 4.

Table 9
Bond critical points and associated properties for various data and models.

Distances (Å), $\rho(\mathbf{r}_c)$ ($\text{e } \text{\AA}^{-3}$), $\nabla^2\rho(\mathbf{r}_c)$ and λ_i ($\text{e } \text{\AA}^{-5}$)

Data/model	From	Dist.	To	Dist.	$\rho(\mathbf{r}_c)$	$\nabla^2\rho(\mathbf{r}_c)$	λ_1	λ_2	λ_3	Ellipticity
295 K	Si	0.744	N2	0.987	1.031	3.637	−6.289	−5.637	15.563	0.116
200 K	Si	0.727	N2	1.003	1.023	3.568	−6.418	−6.349	16.336	0.011
150 K	Si	0.726	N2	1.004	1.052	−3.014	−7.439	−6.005	16.458	0.239
IAM	Si	0.734	N2	0.996	0.721	9.803	−2.618	−2.584	15.005	0.013
DFT	Si	0.699	N2	1.030	0.913	11.390	−5.316	−4.953	21.663	0.068
150 K	Si	0.726	N1	1.009	1.038	2.677	−7.688	−5.935	16.300	0.295
200 K	Si	0.725	N1	1.011	1.022	3.217	−7.211	−6.183	16.610	0.166
295 K	Si	0.743	N1	0.992	0.991	4.753	−5.937	−5.117	15.807	0.160
IAM	Si	0.736	N1	0.999	0.715	9.490	−2.566	−2.525	14.581	0.016
DFT	Si	0.702	N1	1.034	0.886	11.285	−5.115	−4.772	21.174	0.067
150 K	Si	0.721	N1	1.015	0.906	6.007	−5.765	−5.404	17.176	0.067
200 K	Si	0.722	N1	1.015	0.950	4.801	−6.278	−5.847	16.926	0.074
295 K	Si	0.737	N1	1.000	0.963	4.206	−6.433	−5.328	15.967	0.207
IAM	Si	0.736	N1	1.000	0.715	9.502	−2.572	−2.522	14.597	0.020
DFT	Si	0.701	N1	1.035	0.894	11.160	−5.188	−4.837	21.192	0.067
150 K	N2	1.453	N2	1.453	0.109	1.272	−0.314	−0.314	1.901	0
200 K	N2	1.453	N2	1.453	0.121	1.267	−0.264	−0.263	1.794	0
295 K	N2	1.453	N2	1.453	0.104	1.220	−0.189	−0.189	1.598	0
IAM	N2	1.453	N2	1.453	0.114	1.203	−0.085	−0.085	1.373	0
DFT	N2	1.453	N2	1.453	0.108	1.128	−0.195	−0.195	1.520	0

entire triangular face of the N2 atom basin therefore constitutes an interaction surface between pairs of these atoms. The experimental and theoretical densities $\rho(\mathbf{r}_c)$ at this b.c.p. are very close to the IAM value, resembling the pure overlap of non-interacting spheres. The small curvature along the interaction vector (λ_3) emphasizes the weakness of this interaction with respect to the strong Si—N bonds. It reflects the relatively long range of interaction as well as the lower densities involved at these separations. Associated curvatures in the orthogonal plane are also very small.

The DFT and experimental $\Delta\rho(\mathbf{r})_{\text{stat}}$ in the region of the N2—N2 b.c.p. are shown in Figs. 7(d) and (b), respectively. Fig. 7(b) shows that $\Delta\rho(\mathbf{r})_{\text{stat}}$ at the b.c.p. is negative, so that according to DFT the total density at the b.c.p., $\rho(\mathbf{r}_c)$, is depleted with respect to the IAM and the valence p_z density

contracts toward the N2 nuclei. This is consistent with a localized exchange depletion interaction *via* wavefunction overlap. Bader (1998) classifies this as bonding because any redistribution of atomic density that accommodates the interacting atom lowers the energy density, regardless of the amount of energy involved or the relative strengths of the forces involved in maintaining structural equilibrium. In contrast, the 200 K experimental $\Delta\rho(\mathbf{r})_{\text{stat}}$ is mildly positive at the b.c.p., indicating that the p_z density extends weakly into the interaction region. This is suggestive of a closed shell non-bonding interaction with little or no wavefunction correlation at all and close agreement with the non-interacting IAM. However, the experimental b.c.p. densities, $\rho(\mathbf{r}_c)$, are within 1 s.u. ($0.01 \text{ e } \text{\AA}^{-3}$) of the IAM density and 2 s.u.'s of the DFT density.

The theoretical N2—N2 bonding is manifestly weak, of long range, involving very little charge migration and therefore lowering the energy to only a minor extent. It is unlikely to explain the apparent lattice strain leading to the 113° Si—N1—Si bond angles across the mirror plane. A more reasonable scenario would be if the charge migration arising in the vicinity of the fourth b.c.p. occurred through N2—N2 crowding resulting from excessively foreshortened Si—N2 bonds elsewhere in the lattice.

10. Atomic charges

Atomic charges were determined using several different techniques and are shown in Table 10. All these estimates are consistent in terms of chemical expectations, but their differences necessarily reflect the different mechanisms by which they were defined.

Using Hirshfeld partitioning, one of many so-called *fuzzy*-boundary charge-assignment methods (Ghosez *et al.*, 1998), the $\Delta\rho(\mathbf{r})$ residuals from the IAM refinements were projected

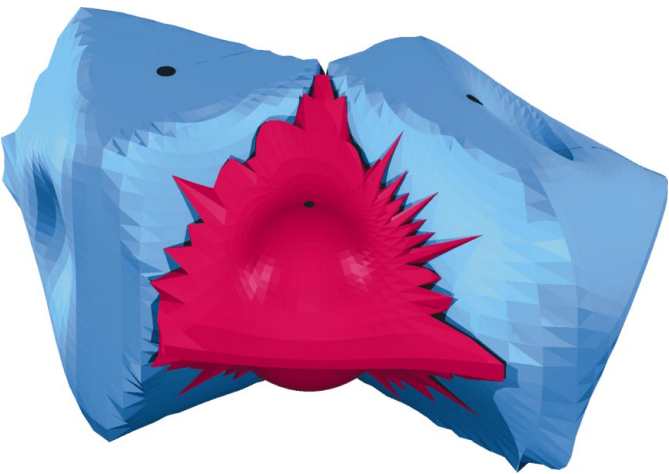


Figure 8
AIM atomic basins represented by the zero-flux surface for which $\nabla\rho(\mathbf{r}) \cdot \mathbf{n}(\mathbf{r}) = 0$ for N2, Si and N1 (in order left to right) and as derived from DFT.

Table 10

Atomic charges (e) determined from Hirshfeld partitioning, GSF monopole sums and integrals within Bader's zero-flux surfaces.

Equivalent charges determined from $P6_3$ models differ by at most 0.01 e.

	Formula multiplicity	AIM promol.	Hirshfeld			GSF monopoles			DFT AIM analysis 0 K	GSF AIM analysis 200 K
			150 K	200 K	295 K	150 K	200 K	295 K		
Si	3	2.45	0.46 (3)	0.46 (3)	0.51 (4)	0.65	0.68	1.27	2.80	2.81
N1	3	-1.31	-0.34(3)	-0.33(4)	-0.35(6)	-0.49	-0.51	-0.95	-2.10	-2.07
N2	1	-1.26	-0.36 (3)	-0.39 (4)	-0.46 (6)				-2.08	-2.18

onto spherically symmetric atomic density basis functions (Spadaccini, 2000). Atomic charges determined in this manner show very good agreement across three experiments and appropriately reflect charge transfer from Si to N. There is a trend toward smaller Hirshfeld charges for N1, although both are equal within 2 s.u.'s.

An alternative measure of charge results from integrating the total electron density within each AIM zero-flux attractor (Flensburg & Madsen, 2000). Charges were calculated for each independent atom of the procrystal. These represent the non-ionizing charge transfer occurring entirely through atomic overlap (Maslen & Etschmann, 2000), *i.e.* an inherent ionic charge. Analogue charges determined from the GSF density at 200 K and the DFT density therefore reflect the total atomic charge transfer in the attractor basins associated with bonding. The latter two charges agree very closely, as might be expected from the $\Delta\rho(\mathbf{r})_{\text{stat}}$ similarities shown in Figs. 4–6. The charges are significantly larger than those from the procrystal and this excess reflects the chemically induced charge transfer associated with bonding.

A third measure of charge was determined from the refined monopole populations of the GSF models. Each atom-centred higher-order pole adds and removes density from the lattice in equal quantities and so has no impact on the charges on the atoms to which they are centred. On the other hand, they can contribute charge to neighbouring atomic centres and so, although the monopole estimates are qualitatively consistent with chemical expectations, there is an inherent ambiguity about the properties they represent.

11. Summary and discussion

The structural properties of the silicon nitrides have been studied by many authors, using many techniques. Here we have presented the results of three high-precision charge-density imaging experiments from two independent crystals, amongst which there were no reproducible deviations from the high-symmetry prototype. Statistical analysis of the normalized structure factors does not discriminate between centrosymmetric and non-centrosymmetric space groups. Neither did determinations of absolute structure on account of the small complex dispersion coefficient. Applying Hamilton's tests to the least-squares refinement *R*-factor strongly favours the non-centrosymmetric model, although with reservations about the method.

The critical positional and mean-square displacement parameters of the $P6_3$ model do not vary systematically

between experiments, despite consistent trends in the non-symmetry critical parameters. The spread of these additional parameters is generally much larger than their associated individual refinement-based standard uncertainties. That is, they are not reproducible even though they apparently have high precision. There was no evidence to suggest twinning or structural instabilities based on the anisotropic displacement parameters. The bond lengths and angles of the low-symmetry models do not differ appreciably from the values of the high-symmetry model, giving little indication of the structural advantages of symmetry breaking. Finally, the charge density imaged at three different temperatures from two different crystals shows greater variation than that between the two symmetries at each temperature.

From the forgoing analysis, we were unable to categorically exclude the low-symmetry hypothesis. Random and systematic experimental errors were sufficiently large to preclude convergence of the low-symmetry IAM refinements to systematic values. On the other hand, to the precision attained, there seems to be little profit in rejecting the high-symmetry structure, since it models the three experiments far more consistently. The strongest external evidence of broken symmetry comes from the CBED study of Bando (1983). CBED is a very powerful technique for probing the crystal symmetry. On the other hand, Johnson (1972) showed that the symmetry observed in a CBED diffraction pattern depends on the symmetry of the scattering crystal as a whole and not just that of the unit cell. In pyrolytic graphite the true $P6_3/mc$ symmetry was shown to reduce to $R\bar{3}m$ by shifting the focal point of the electron beam into the vicinity of the stacking faults. It is quite plausible that Bando (1983) encountered a similar phenomenon.

The crystals used in both the Goodman & O'Keeffe (1980) and Bando (1983) studies were prepared identically from a 50% mixture of both α - Si_3N_4 and β - Si_3N_4 phases heated to 1973 K for 10 h. The α - Si_3N_4 and β - Si_3N_4 phases have closely related structures and unit-cell parameters, as discussed in depth by Grün (1979). It is not inconceivable that residual stacking faults remained after the annealing process. In fact, we recently learnt of new CBED evidence for $P6_3/m$ symmetry determined by Tsuda & Tanaka (2003) in the process of reviewing a forthcoming edition of *International Tables* (Vol. B, 2001, edited by U. Shmueli).

We therefore suggest that $P6_3/m$ symmetry could be adopted for β - Si_3N_4 without any loss of structural precision, as initially suggested by Wild *et al.* (1972), later confirmed by Goodman & O'Keeffe (1980) and, more recently, supported

by density-functional theory calculations involving structural relaxation by Belkada *et al.* (2002).

With the symmetry ambiguity addressed, the focus was directed towards electron density. Although the topography of the charge density strongly resembles that expected for a covalently bound crystal, the topology of the total density, as characterized by the bond critical points, implies strong ionic character. This was supported by all atomic charge estimates applied and in particular the AIM analysis of the IAM procystal density.

The broken $\bar{6}m2$ symmetry (D_{3h}) of the $\Delta\rho(\mathbf{r})$ and $\Delta\rho(\mathbf{r})_{\text{stat}}$ around the N1 site, and the compression of the unique Si—N1—Si bond angle from 120 to 113° accompanied by broken coplanarity with its three Si neighbours, strongly suggest that the lattice is under some form of internal strain. This strain in turn should have a strong bearing on its bulk modulus and other physical properties. However, the multipolar and topological analyses of the electron density presented here have not provided any immediate clues as to why such lattice strain is favoured. The improved accuracy of the experimental atomic coordinates described herein may well provide a more precise foundation for further theoretical-based lattice relaxation studies.

This study was supported by a grants-in-aid for Scientific Research in Priority Areas (B) No. 740, and No. 14550663 from the Ministry of Education, Culture, Sports, Science and Technology, Japan. DDB acknowledges a grant-in-aid for JSPS fellows, No. P02148 from the Ministry of Education, Culture, Sports, Science and Technology, Japan. We would also like to thank A. Kirfel for valued comments made whilst in Geneva at the XIX IUCr congress.

References

- Abrahams, S. C., Schmalle, H. W., Williams, T. A., Reller, F. L., Widmer, D., Bednorz, J. G., Spreiter, R., Bosshard, C. & Günter, P. (1998). *Acta Cryst.* **B54**, 399–416.
- Bader, R. (1998). *J. Phys. Chem. A*, **102**, 7314–7323.
- Bader, R. F. W. (1990). *Atoms in Molecules: A Quantum Theory*. Oxford: Clarendon Press.
- Bando, Y. (1983). *Acta Cryst.* **B39**, 185–189.
- Belkada, R., Kohyama, M., Shibayanagi, T. & Naka, M. (2002). *Phys. Rev. B*, **64**, 1–4.
- Belkada, R., Shibayanagi, T., Naka, M. & Kohyama, M. (2000). *J. Am. Ceram. Soc.* **83**, 2449–2454.
- Boese, R., Niederprüm, N., Bläser, D., Maulitz, A. H., Antipin, M. Y. & Mallinson, P. (1997). *J. Phys. Chem. B*, **101**, 5794–5799.
- Borgen, O. & Seip, H. M. (1961). *Acta Chem. Scand.* **15**, 1789.
- Ching, W., Ouyang, L. & Gale, J. D. (2000). *Phys. Rev. B*, **61**, 8696–8700.
- Ching, W. Y., Huang, M. Z. & Mo, S.-D. (2000). *J. Am. Ceram. Soc.* **83**, 780–786.
- Clementi, E. & Roetti, C. (1974). *At. Nucl. Data Tables*, **14**, 177–478.
- Coppens, P. (1998). *Acta Cryst.* **A54**, 779–788.
- Desclaux, J. P. (1969). *Comput. Phys. Commun.* **1**, 216–222.
- Downs, R. T., Gibbs, G. V., Boisen Jr, M. B. & Rosso, K. M. (2002). *Phys. Chem. Miner.* **29**, 369–385.
- Draper, N. R. & Smith, H. (1981). *Applied Regression Analysis*, 2nd Ed. New York: John Wiley.
- Flack, H. (1983). *Acta Cryst.* **A39**, 879–881.
- Flack, H. & Bernardinelli, G. (2000). *J. Appl. Cryst.* **33**, 1143–1148.
- Flensburg, C. & Madsen, D. (2000). *Acta Cryst.* **A56**, 24–28.
- Furuya, K., Matsuo, K., Munakata, F., Akimune, Y., Ye, J., Yamamoto, Y. & Ishikawa, I. (1999). *J. Mater. Res.* **14**, 1690–1691.
- Ghosez, P., Michenaud, J.-P. & Gonze, X. (1998). *Phys. Rev. B*, **58**, 6224–6240.
- Goodman, P. & O'Keeffe, M. (1980). *Acta Cryst.* **B36**, 2891–2893.
- Grün, R. (1979). *Acta Cryst.* **B35**, 800–804.
- Hall, S. R., du Boulay, D. & Olthof-Hazekamp, R. (2003). *Gnu Xtal*, System 3.7.2. University of Western Australia.
- Hamilton, W. C. (1965). *Acta Cryst.* **18**, 502–510.
- Hansen, N. K. & Coppens, P. (1978). *Acta Cryst.* **A34**, 909–921.
- Hardie, D. & Jack, K. H. (1957). *Nature*, **180**, 332–333.
- Hirshfeld, F. L. (1977). *Isr. J. Chem.* **16**, 198–201.
- Jack, K. H. & Wilson, W. I. (1972). *Nature (London)*, **238**, 28–29.
- Johnson, C. K. (1971). *ORTEP*. Report ORNL-3794, revised. Oak Ridge National Laboratory, Tennessee, USA.
- Johnson, A. (1972). *Acta Cryst.* **A28**, 89–91.
- Kato, K., Inoue, Z., Kijima, K., Kawada, I., Tanaka, H. & Yamane, T. (1975). *J. Am. Ceram. Soc.* **58**, 90–91.
- Kirfel, A., Krane, H.-G., Blaha, P., Schwarz, K. & Lippman, T. (2001). *Acta Cryst.* **A57**, 663–677.
- Kishimoto, S., Ishizawa, N. & Vaalsta, T. P. (1998). *Rev. Sci. Instrum.* **69**, 384–391.
- Liu, A. Y. & Cohen, M. L. (1989). *Science*, **245**, 841.
- Liu, A. Y. & Cohen, M. L. (1990). *Phys. Rev. B*, **41**, 10727–10734.
- Maslen, E. N. & Etschmann, B. E. (2000). *Aust. J. Phys.* **53**, 299–316.
- Matsunaga, K. & Iwamoto, Y. (2001). *J. Am. Ceram. Soc.* **84**, 2213–2219.
- Matsunaga, K., Iwamoto, Y. & Matsubara, H. (2000). *J. Mater. Res.* **15**, 429–436.
- Mo, S.-D., Ouyang, L. & Ching, W. Y. (1999). *Phys. Rev. Lett.* **83**, 5046–5049.
- Ogata, S., Hirotsaki, N., Kocer, C. & Shibutani, Y. (2003). *J. Mater. Res.* **18**, 1168–1172.
- Perdew, J., Burke, S. & Ernzerhof, M. (1996). *Phys. Rev. Lett.* **77**, 3865.
- Sasaki, S. (1989). *KEK Rep.* **88**, 1–136.
- Sasaki, S. (1990). *KEK Rep.* **90**, 1–143.
- Satow, Y. & Iitaka, Y. (1989). *Rev. Sci. Instrum.* **60**, 2390–2393.
- Schneider, J., Frey, F. K. & Laschke, N. J. (1994). *Z. Kristallogr.* **209**, 328–333.
- Schwarz, K., Blaha, P. & Madsen, G. (2001). *Comput. Phys. Commun.* **147**, 71–76.
- Schwarzenbach, D., Abrahams, S. C., Flack, H. D., Gonschorek, W., Hahn, T., Huml, K., Marsch, R. E., Prince, E., Robertson, B. E., Rollett, J. S. & Wilson, A. J. C. (1989). *Acta Cryst.* **A45**, 63–75.
- Spackman, M. A. (1986). *Acta Cryst.* **A42**, 271–281.
- Spackman, M. A., Hill, R. J. & Gibbs, G. V. (1987). *Phys. Chem. Miner.* **14**, 139–150.
- Spadaccini, N. (2000). *Gnu Xtal*, System 3.7.2, edited by S. R. Hall, D. J. du Boulay & R. Olthof-Hazekamp. University of Western Australia.
- Stewart, R. F. (1977). *Isr. J. Chem.* **16**, 124–131.
- Stewart, R. F. (1980). *Electron and Magnetization Densities in Molecules and Crystals*, edited by P. Becker, pp. 427–431. New York: Plenum Press.
- Stewart, R. F., Spackman, M. A. & Flensburg, C. (2000). *Valray2.1 User's Manual*. Carnegie-Mellon University, Pittsburgh, USA, and University of Copenhagen, Denmark.
- Streltsov, V. A., Belokoneva, E. L., Tsirelson, V. G. & Hansen, N. K. (1993). *Acta Cryst.* **B49**, 147–153.
- Tsuda, K. & Tanaka, M. (2003). Personal Communication.
- Vaalsta, T. P. & Hester, J. R. (1997). *Diff14A*. Photon Factory, Tsukuba.
- Vogelgesang, R., Grimditch, M. & Wallace, J. (2000). *Appl. Phys. Lett.* **76**, 982–984.
- Wild, S., Grieseson, P. & Jack, K. H. (1972). *Spec. Ceram.* **5**, 385–393.
- Zachariasen, W. H. (1967). *Acta Cryst.* **23**, 558–564.

- Zerr, A., Miehe, G., Serghiou, G., Schwarz, M., Kroke, E., Riedel, R., Fueß, H., Kroll, P. & Böhler, R. (1999). *Nature (London)*, **400**, 340–342.
- Zhao, G. N. & Bachlechner, M. E. (1998). *Phys. Rev. B*, **58**, 1887–1895.
- Zhuo, J. M., Blaha, P. & Schwarz, K. (1997). *J. Phys. Condens. Matter*, **9**, 7541–7561.
- Zucker, U. H. & Schulz, H. (1982). *Acta Cryst.* **A38**, 563–568.